

Copyright © 2013, Paper 17-013; 45117 words, 6 Figures, 0 Animations, 1 Tables.
<http://EarthInteractions.org>

Effects of Topography on Assessing Wind Farm Impacts Using MODIS Data

Liming Zhou*

Department of Atmospheric and Environmental Sciences, University at Albany,
State University of New York, Albany, New York

Yuhong Tian

IMSG, NOAA/NESDIS/STAR, College Park, Maryland

Haishan Chen

Key Laboratory of Meteorological Disaster, Ministry of Education, Nanjing University
of Information Science and Technology, Nanjing, China

Yongjiu Dai

School of Geography, Beijing Normal University, Beijing, China

Ronald A. Harris

Department of Atmospheric and Environmental Sciences, University at Albany,
State University of New York, Albany, New York

Received 17 December 2012; accepted 27 June 2013

* Corresponding author address: Liming Zhou, Department of Atmospheric and Environmental Sciences, University at Albany, State University of New York, 1400 Washington Avenue, Albany, NY 12222.

E-mail address: lzhou@albany.edu

ABSTRACT: This paper uses the empirical orthogonal function (EOF) analysis to decompose satellite-derived nighttime land surface temperature (LST) for the period of 2003–11 into spatial patterns of different scales and thus to identify whether (i) there is a pattern of LST change associated with the development of wind farms and (ii) the warming effect over wind farms reported previously is an artifact of varied surface topography. Spatial pattern and time series analysis methods are also used to supplement and compare with the EOF results. Two equal-sized regions with similar topography in west-central Texas are chosen to represent the wind farm region (WFR) and nonwind farm region (NWFR), respectively. Results indicate that the nighttime warming effect seen in the first mode (EOF1) in WFR very likely represents the wind farm impacts due to its spatial coupling with the wind turbines, which are generally built on topographic high ground. The time series associated with the EOF1 mode in WFR also shows a persistent upward trend over wind farms from 2003 to 2011, corresponding to the increase of operating wind turbines with time. Also, the wind farm pixels show a warming effect that differs statistically significantly from their upwind high-elevation pixels and their downwind nonwind farm pixels at similar elevations, and this warming effect decreases with elevation. In contrast, NWFR shows a decrease in LST with increasing surface elevation and no warming effects over high-elevation ridges, indicating that the presence of wind farms in WFR has changed the LST–elevation relationship shown in NWFR. The elevation impacts on Moderate Resolution Imaging Spectroradiometer (MODIS) LST, if any, are much smaller and statistically insignificant than the strong and persistent signal of wind farm impacts. These results provide further observational evidence of the warming effect of wind farms reported previously.

KEYWORDS: Wind farm impact; Empirical orthogonal function; Land surface temperature

1. Introduction

Climate change is one of the most serious environmental issues of our time. Wind power as an alternative clean energy source to fossil fuels supports environmental sustainability and possibly provides part of the solution to our energy security problem (Pacala and Socolow 2004; NRC 2007; Pryor and Barthelmie 2011). The use of wind power in the United States and other countries like China, Germany, Spain, and India has experienced continuous growth in recent years. Wind energy currently amounts to $\sim 3\%$ of U.S. electricity generation (AWEA 2012; U.S. DOE 2012) and could supply up to 20% of the total U.S. electricity by 2030 (U.S. DOE 2008). To generate this substantial amount of energy, wind farms would have to install a huge number of wind turbines over a continental-scale area (Wang and Prinn 2010; Fiedler and Bukovsky 2011).

Wind power depends on weather and climate, and wind farms, if large enough, might also modify the weather and climate, at least in their immediate vicinity. While converting wind's kinetic energy into electrical power, wind turbines modify surface fluxes of heat, momentum, moisture, and CO_2 exchanges in the atmospheric boundary layer (ABL) (Rajewski et al. 2013) and enhance turbulence in their rotor wakes, thus increasing the vertical mixing within ABL (Baidya Roy and Traiteur 2010). The net effect should be small and local for a limited number of wind turbines but may become noticeable if hundreds or thousands of wind

turbines are installed over a particular region. During the past few years a growing number of numerical simulations using global and regional models with hypothetical wind farms have generally agreed that wind farms can affect local to regional weather and climate (e.g., Keith et al. 2004; Kirk-Davidoff and Keith 2008; Wang and Prinn 2010; Fiedler and Bukovsky 2011; Fitch et al. 2013). However, these studies are primarily in the model domain, with limitations and uncertainties due to the use of simple subgrid-scale wind turbine parameterizations and the lack of observations for validation.

Increasing scientific and public interests in assessing environmental consequences of wind farms highlight the need to understand the detailed processes of observed meteorological fields at wind farm/turbine scales (Rajewski et al. 2013) and to develop the modeling capability to characterize wind turbine–atmosphere interactions in numerical models. Doing so requires high-resolution observations (in both space and time) over operating wind farms. However, the general structure and functioning of wind farms, wind turbine parameters, and meteorological observations within wind farms are proprietary and thus not available to the public. Furthermore, most wind farms are not within the synoptic weather observational network, which makes the use of conventional meteorological data challenging.

The availability of high-resolution remote sensing data provides an observational approach to detect, quantify, and attribute wind farm impacts with spatial detail. Satellite-derived land surface temperature (LST) measures the temperature of Earth's surface thermal emission. LST has a stronger day–night variation than surface air temperatures from daily weather reports and thus is more sensitive to changes in surface conditions (Jin and Dickinson 2002; Imhoff et al. 2010). Zhou et al. (Zhou et al. 2012) find a nighttime warming effect over large wind farms in west-central Texas using winter and summer mean LSTs derived from the Moderate Resolution Imaging Spectroradiometer (MODIS). Zhou et al. (Zhou et al. 2013) provides further observational evidence of this warming effect by analyzing diurnal and seasonal variations of MODIS LST anomalies with more observations under different quality controls.

The wind turbines in the study region of Zhou et al. (Zhou et al. 2012; Zhou et al. 2013) are generally built on mountain ridges that overlap with the reported warming effect. This raises a critical question of whether this warming effect is an artifact of topography. Mountains affect climate by changing the patterns of temperature, wind circulation, and precipitation (Minder et al. 2010). While variations in elevation, terrain slope, and aspect angles can interact with satellite viewing geometry to cause biases in retrieved LSTs (Lipton and Ward 1997; Liu et al. 2009), only the elevation effect and zenith angle changes were corrected in the routine retrieval in the MODIS LSTs (Wan and Li 1997; Wan 2006). Hence, some residual topographic effects may still exist in the MODIS LSTs. Furthermore, using satellite data to detect and quantify wind farm impacts is still in the exploratory stage. LST variations over an operational wind farm contain not only the local wind turbine effect but also the variability controlled by surface properties (Zhang et al. 2010; Imhoff et al. 2010) and large-scale meteorological conditions (Zhou et al. 2012). Separating the local versus regional- to large-scale variability of the MODIS LSTs is crucial to uncovering the wind farm effect. To identify and quantify the wind farm impacts, Zhou et al. (Zhou et al. 2012) simply use the areal mean LST differences (i) between two periods and (ii) between wind farm pixels and nearby

nonwind farm pixels, while the topographic effect on LST has to be assessed at the pixel level. In addition, LSTs also contain uncertainties due to residual atmospheric effects and errors from observations and retrievals (Wan 2006). Therefore, considering the significant implications of this finding, it is necessary to use other approaches to verify that the reported warming effect over wind farms is not an artifact of varied surface topography.

Here we use an empirical orthogonal function (EOF) analysis to explore the structure of LST variability from MODIS, identify the spatial patterns of variability (EOF modes) and their time variations (EOF time series), and give a measure of the “importance” of each pattern. We choose EOF analysis for its potential to evaluate the spatial pattern of LST changes. EOF determines a set of orthogonal functions that characterizes the covariability of time series for a set of grid points. The degree of spatial covariability may help uncover underlying processes of changes detected by using satellite data (e.g., Zhou et al. 2001). Pixels with strong spatial covariance reflect similar year-to-year LST changes. If changes in LST are due to variations of surface topography, we would expect to see a high degree of spatial covariability over regions with similar elevations. If LST variations are dominated by a randomly distributed (in space) effect such as data noise, we would expect pixels to show differences in LST variations that lack spatial coherence. If changes in LST are due to the presence of operational wind turbines, we would expect a high degree of spatial covariability over pixels with wind turbines. However, we realize that MODIS time series might be too short to draw any definite conclusions based on EOF analysis alone. Therefore, the approaches of spatial pattern and time series analysis in Zhou et al. (Zhou et al. 2012; Zhou et al. 2013) are also used to supplement and compare with the EOF results but with an emphasis on the topographic effect at pixel level, which was not done previously.

The objective of this paper is threefold. First, it aims to find whether the EOF approach can decompose the LSTs into spatial patterns of different scales and thus help to identify whether there is a pattern associated with the development of wind farms. Second, it serves as a detailed analysis to examine whether the warming effect over wind farms reported by Zhou et al. (Zhou et al. 2012) is primarily due to varied topography at pixel level. Third, it explores EOF as a different approach to verify whether the results of Zhou et al. (Zhou et al. 2012) are robust.

2. Data and methods

2.1. Study region

We choose two equal-sized regions in west-central Texas that are close to each other and share similar topography in terms of elevation, slope, and orientation of terrain features, one with wind farms and the other without wind farms, which are referred to as the wind farm region (WFR) and the nonwind farm region (NWFR), respectively. The WFR (32.1°–32.9°N, 101°–99.8°W; Figure 1) had 2358 wind turbines installed by 2011, with ~90% completed by 2008. The wind turbines are identified geographically based on the database of the Federal Aviation Administration (FAA) (Zhou et al. 2012) and verified via Google Earth (Zhou et al. 2013). As there are several other wind farms near WFR, it is impossible to find a NWFR without any wind turbines. Instead, we identify a region (30.5°–31.3°N,

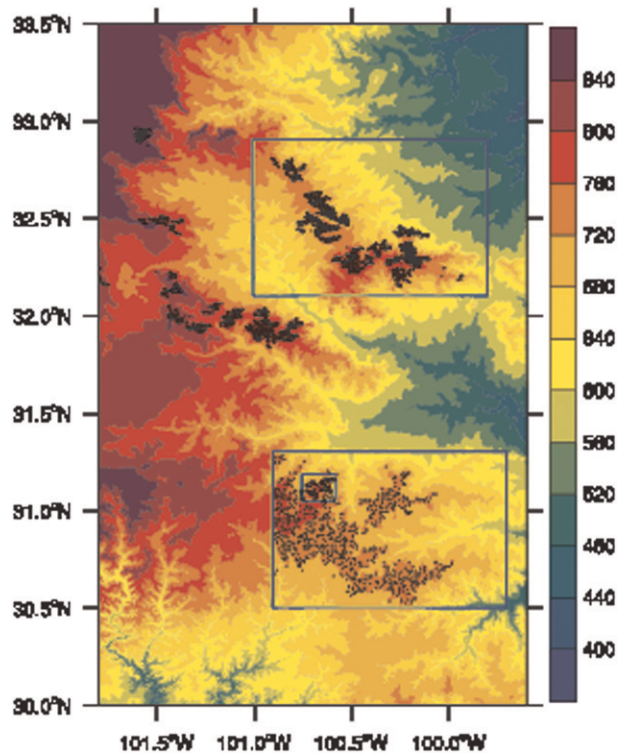


Figure 1. Elevation (m) map of west-central Texas that contains WFR (upper box) and NWFR (lower box) at spatial resolution of 30 arc-s (~1.0 km). Cluster pixels in black with a plus symbol are wind turbines: 2358 in WFR (32.1°–32.9°N, 101°–99.8°W) and 99 (the inner rectangle) in NWFR (30.5°–31.3°N, 100.9°–99.7°W). The pixels in black with a plus symbol outside the inner rectangle in NWFR are AWFPs.

100.9°–99.7°W; Figure 1) to the south of WFR as NWFR that has 99 wind turbines built in and after 2009. The presence of these 99 wind turbines is expected to have a very limited impact on LST in NWFR because (i) the total number of wind turbines is small and (ii) most of the wind turbines are likely operating only in the last 1–2 years of the study period. WFR consists of four of the world’s largest wind farms and has the highest concentration of wind turbines in west-central Texas. Particularly, the majority of the wind turbines were built between 2005 and 2008, which makes it possible to use ~10 years of MODIS data. For other wind farms near WFR, most wind turbines were installed recently, making it too short to investigate their impacts on LSTs.

2.2. Data processing

The collection-5 MODIS 8-day-average 1-km LST images are aggregated spatially and temporally into seasonal [December–February (DJF) and June–August (JJA)] and annual (ANN) means and anomalies at 0.01° resolution for the period

of 2003–11, as done by Zhou et al. (Zhou et al. 2013). The MODIS LST data have been proven to be of high quality in a variety of studies (Wan 2006). The LST images consist of four acquisitions (~ 1030 and ~ 1330 local solar time at daytime and ~ 2230 and ~ 0130 local solar time at nighttime) and have quality assurance (QA) values for each image. For simplicity, we will not consider daytime LSTs and QA information of MODIS LSTs in the present analysis because the impacts of wind farms on LST (i) are too small to be detected at daytime and (ii) differ only slightly under different QA controls (Zhou et al. 2013). We also combine the two LSTs at ~ 2230 and ~ 0130 local solar time to produce one average nighttime LST to reduce data uncertainties/noise and only consider the MODIS LSTs with a whole year of data (Zhou et al. 2012). Furthermore, we show primarily the results of JJA at nighttime when the wind farm impacts are largest but also supplement our analysis with some results in DJF and ANN. DJF represents the season with the least wind farm impact. In total, there are nine images (from 2003 to 2011) for every season (DJF, JJA, and ANN) in each study region (WFR and NWFR) and each image has 9600 pixels (120 columns \times 80 lines).

The wind turbines in WFR are generally built on mountain ridges, with an average elevation of 749.1 ± 21.4 m based on the wind turbine site elevation data of FAA (Figure 1). The 99 wind turbines in NWFR are also located in mountain ridges (Figure 1). The global 30 arc-s elevation dataset (GTOPO30) global digital elevation map with a horizontal grid spacing of 30 arc-s (~ 1.0 km) was downloaded online (from http://eros.usgs.gov/#/Find_Data/Products_and_Data_Available/gtopo30_info). We reproject the elevation data into the 0.01° pixels as done for the MODIS LSTs. In total, there are 890 pixels with at least one wind turbine, referred to as wind farm pixels (WFPs), in WFR and 51 WFPs in NWFR at the 0.01° resolution (Figure 1). We plan to compare the LST changes of WFPs between WFR and NWFR, but the sample size of the latter is too small and so we artificially designate some pixels as “wind farms” in NWFR following the elevation histogram of real wind farms in WFR (Figure 2a). Among the 9600 pixels, we choose 2276 with an elevation greater than 712 m (>76 th percentile) in WFR and 1920 with an elevation greater than 731 m (>80 th percentile) in NWFR as high-elevation pixels. These pixels generally represent the site elevations of wind turbines as 734 out of 890 WFPs (i.e., 82.5%) belong to the 2276 high-elevation pixels in WFR. Note that the wind turbines in WFR were mostly built over ridges whose elevations are higher than their surroundings across the study region, not only over the highest ridge pixels in the northwestern WFR (Figure 1). The 76th and 80th percentile thresholds are chosen so that two groups of pixels defined in the next paragraph will have a similar number of pixels and a similar elevation distribution as the real wind farm pixels.

To resemble the real wind turbines over high elevations, we randomly choose 849 pixels from the 1920 high-elevation pixels in NWFR. To differentiate these pixels from real WFPs, we refer to these 849 pixels plus 51 WFPs (in total 890 pixels) as artificial wind farm pixels (AWFPs) in NWFR (Figure 1). These 849 pixels are chosen randomly instead from a particular area because it is difficult to justify the choice of one area over another. The presence of wind turbines will have an effect on their downwind pixels. For WFR, we further choose 898 pixels from the 2276 high-elevation pixels that are located in the upwind direction of wind farms (i.e., in the east and south of WFPs) to exclude the downwind effect of WFPs.

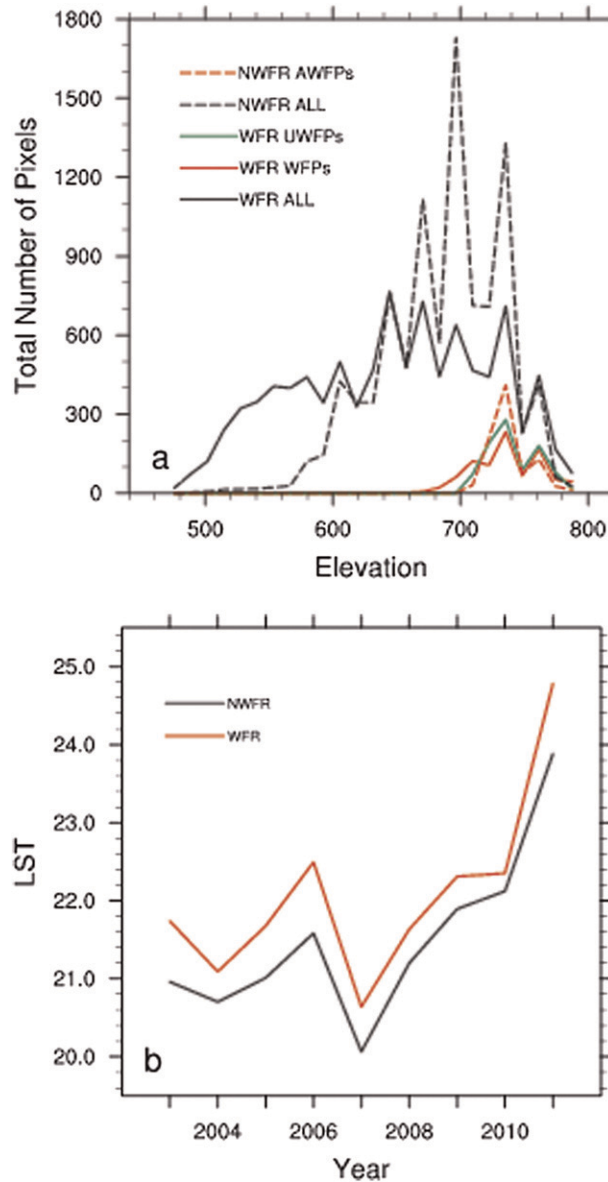


Figure 2. (a) Histogram of surface elevation for all of the pixels and UWFPs, WFPs, and AWFPs and (b) time series of regional mean JJA nighttime LST anomalies ($^{\circ}\text{C}$) averaged over the entire study region in WFR and NWFR for the period of 2003–11.

We refer to these 898 pixels as upwind wind farm pixels (UWFPs). Note that we would prefer to choose exactly 890 UWFPs to match the 890 WFPs but there are several pixels with the same elevation. At the 0.01° resolution, the average elevation is 738.3 ± 27.5 m for WFPs, 737.3 ± 15.9 m for AWFPs, and 741.6 ± 19.4 m for UWFPs. WFR has a larger standard deviation because of its broader elevation range than NWFR. The elevation histogram of WFPs, AWFPs, and UWFPs is shown in Figure 2a.

To quantify the wind farm impact, Zhou et al. (Zhou et al. 2012) compared the LSTs of 890 WFPs with 1538 nearby nonwind farm pixels for WFR. For NWFR, we randomly choose 1538 pixels around the 890 AWFs following the elevation histogram of the 1538 pixels in WFR as their corresponding nearby nonwind farm pixels. At the 0.01° resolution, the average elevation for these 1538 pixels is 661.2 ± 55.6 m in WFR and 661.7 ± 14.8 m in NWFR.

2.3. Methods

The LST variations consist of two components: the background regional- or large-scale variability signal (referred to as regional interannual variability) and the subregional-scale variability. The former is much larger than the latter in magnitude and is irrelevant to wind farms. Particularly, the two study regions are small and close to each other, and thus their pixels should share a similar background signal. Figure 2b shows the regional mean JJA nighttime LST anomalies averaged over the entire domain in WFR and NWFR, respectively, for the period of 2003–11. The study regions exhibit strong year-to-year variations, with the coldest year in 2007 and the warmest year in 2011 when the historic Texas drought occurred (Karl et al. 2012). Evidently, WFR and NWFR have gone through similar meteorological conditions from 2003 to 2011 and have been getting warmer since 2007. Because our analysis is interested in the variability on spatial scales smaller than regional, we remove this background regional interannual variability signal from the MODIS LST anomalies created in section 2.2 for each LST image. In other words, we subtract the same regional mean LST anomaly (one value per image) from the MODIS LST anomaly for every pixel in each year to emphasize the pixel-level LST spatial variability. Note that the resulting LST change represents a change relative to the regional mean value and is denoted as Δ LST.

Three different methods are used to quantify the topographic effect on LSTs over our study regions. The first method (method I) applies a simple EOF analysis to the MODIS Δ LSTs. The EOF method has been extensively used to analyze the spatial and temporal variability of geophysical fields by decomposing the data into a set of orthogonal basis functions (Bjornsson and Venegas 1997). Its goal is to express the signal in terms of a relatively small number of EOFs to describe as much of the original information as possible. The EOF modes show the spatial structure of the major factors that can account for the temporal variations, which represent spatial variability or “modes of variability.” The EOF time series tells us how the amplitude of each EOF mode varies with time. The first few EOFs may explain the majority of the data variance and thus the inversion of the EOF transform using only the first few EOFs provides a noise-filtered dataset.

Note that, even though the EOF method breaks the data into modes of variability, these modes are primarily data modes and not necessarily “physical modes,” and whether they are physical is a matter of subjective interpretation (Bjornsson and Venegas 1997). The first EOF mode would explain more than 94% of the total Δ LST variance in WFR and NWFR if one simply performed the EOF analysis using the MODIS LST anomalies. For this case, EOF1 would represent primarily the climatology of Δ LST and its time series would represent the regional mean LST anomalies from 2003 to 2011 (as shown in Figure 2b). This explains why we remove the background regional interannual variability signal from the MODIS LST

anomalies as described above. One similar example for doing so is the removal of the seasonal cycle of meteorological data before performing EOF analysis, as this signal dominates everything else (Bjornsson and Venegas 1997).

The second and third methods (methods II and III) are adopted from the spatial pattern and time series analyses over WFR in Zhou et al. (Zhou et al. 2012; Zhou et al. 2013) but are used here as a new analysis of topographic effects on LST to primarily supplement and compare with the EOF results over both WFR and NWFR given the short record of the MODIS data. Method II simply calculates the Δ LST differences at pixel level between two periods, 2009–11 and 2003–05 (the last 3 years versus the first 3 years of data), and examines their spatial coupling with wind turbines. This method is reasonable as there are only 111 wind turbines in 2003 but 2358 in 2011 over WFR. Note that the Δ LST differences between two individual years (2010 minus 2003) are also examined in Zhou et al. (Zhou et al. 2012) but will not be used here, as the results are similar to the differences between the two periods. Method III quantifies the areal mean Δ LST differences between WFPs (AWFPs) and their nearby nonwind farm pixels in WFR (NWFR) from 2003 to 2011, as done in urban heat island studies (Zhou et al. 2012). Zhou et al. (Zhou et al. 2013) used three different approaches to quantify Δ LST but obtained consistent results. Here we simply use one of the approaches, the total trend (trend per year \times 8 years of intervals) estimated from the least squares fitting, as the number of operational wind turbines has increased with time since 2003.

3. Results and discussion

To understand how LST changes with varied elevation, we examine the spatial patterns of the surface elevation and the JJA nighttime LST climatology over WFR and NWFR. As expected, LST drops with elevation increase (Liu et al. 2009; Minder et al. 2010) and so the valleys and plains are generally warmer than the ridges and the lowest temperatures are observed in the highest elevations (figures omitted for brevity). The spatial correlation coefficient between elevation and LST is -0.6 for WFR and -0.46 for NWFR, which are statistically significant given the large size of samples ($p \ll 0.05$; $n = 9600$ pixels). The correlation is not close to 1 as spatial variations in land surface properties other than surface elevation (e.g., vegetation amount and type) also play a role in determining the climatology of LST.

The first three EOF modes explain more than 66.6% of the total Δ LST variance for both regions: 29.1%, 22.4%, and 15.1% for WFR and 34.6%, 18.4%, and 13.8% for NWFR. For WFR, there is a strong spatial coupling in EOF1 between positive Δ LSTs and WFPs (Figure 3a), and the corresponding time series (more discussion below) shows a persistent upward trend from 2003 to 2011. Positive Δ LSTs are also seen in lower-elevation plain pixels in the northeastern part of WFR, but they are much weaker in magnitude and spatially smaller than those in WFPs. For NWFR, there is a weak spatial coupling between positive Δ LST and southern lower-elevation valleys in EOF1 (Figure 3b), and the time series does not show an evident trend from 2003 to 2009 (more discussion below). Negative Δ LSTs in EOF1 are generally located over northern ridge pixels of NWFR (Figure 3b) and the western part of WFR (Figure 3a). Overall, EOF1 and its time series show a warming effect over higher-elevation WFPs in WFR but over lower-elevation valleys in NWFR. EOF2 and EOF3 in WFR represent the spatial patterns of higher

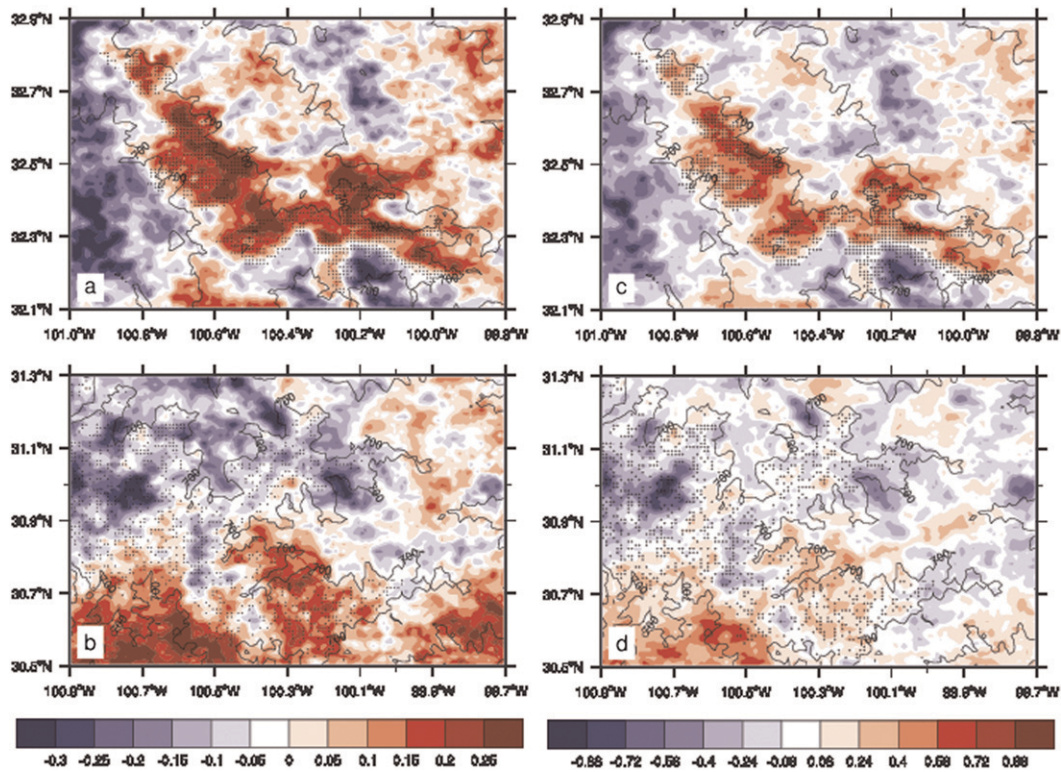


Figure 3. EOF1 of MODIS JJA nighttime Δ LST ($^{\circ}$ C) in (a) WFR and (b) NWFR for the period of 2003–11 and differences (2009–11 minus 2003–05 averages) of MODIS JJA nighttime Δ LST ($^{\circ}$ C) in (c) WFR and (d) NWFR. Pixels with a plus symbol are WFPs in WFR and AWFPs in NWFR. Note that (c) and Figure 2a differ slightly from Figure 2a of Zhou et al. (Zhou et al. 2012), as the latter was calculated from the JJA LST means.

Δ LSTs over lower elevations in the northeastern and southwestern parts of WFR, respectively, and their time series indicate a large interannual variation. There is no spatial coupling between the wind farms and Δ LSTs in EOF2 and EOF3 (figures not shown for brevity).

As mentioned above, the EOF modes are primarily data modes and not necessarily physical modes. To further attribute the EOF1 mode and its time series to the development of wind farms, we compared our results to those in Zhou et al. (Zhou et al. 2012). We use method II to calculate the Δ LST differences (2009–11 minus 2003–05 averages) over WFR (Figure 3c) and NWFR (Figure 3d). The spatial coupling between the warming effect and the wind turbines is evident in Figure 3c and this coupling is well captured by the EOF1 mode (Figure 3a), while there are no warming effects related to topography over NWFR in both Figures 3b and 3d. In general, EOF1 captures the major variations of Δ LST, as also indicated by the percentage of variance explained. If the warming effect of WFPs in EOF1 over WFR was an artifact of topography, we would observe a similar warming effect of AWFPs in EOF1 over NWFR. Furthermore, unlike EOF1 in WFR, EOFs 2 and 3 in

WFR and EOFs 1 and 2 in NWFR generally show negative Δ LSTs over higher elevations, consistent with the observational decrease of temperature with altitude (Liu et al. 2009; Minder et al. 2010).

Next we examine how the Δ LST vary as a function of surface elevation within pixels. All of the 9600 pixels in the two study regions are divided equally into 10 bins in terms of surface elevation, with each bin having \sim 960 pixels. Note that some bins may have several pixels more or less than 960 because not every pixel has a different elevation. For each bin, we also consider two subgroups (WFPs and UWFPs) in WFR and one subgroup (AWFPs) in NWFR, if there are more than 50 pixels present for each subgroup. The corresponding box-and-whisker chart of EOF1 in WFR (Figure 4a) indicates that the minimum, 25th percentile, median, and 75th percentile Δ LSTs are always larger than those of pixels in similar elevation bins, suggesting a warming effect over WFPs relative to their similar surroundings. However, EOF1 of NWFR (Figure 4b) shows similar Δ LSTs in both AWFPs and other pixels with similar elevation bins, suggesting no differences between AWFPs and their similar surroundings. Also, it is interesting to note that the Δ LST generally decreases with elevation for all of the 10 bins in NWFR and also for an elevation lesser than 700 m in WFR. However, the Δ LST increases with an elevation greater than 700 m with the presence of wind turbines in WFR. This increase in WFR differs from NWFR and overlaps with the elevations where the wind farms are built, mainly because of the downwind effects of wind farms over pixels that are close to wind farms but have no wind turbines (Figures 3a,c). This can be seen clearly from the Δ LST changes in UWFPs (Figure 4a). Figures 4c and 4d illustrate the corresponding box-and-whisker chart of the Δ LST differences between the averages of 2009–11 and those of 2003–05 as a function of elevation for WFR and NWFR using method II. Again, WFPs are generally associated with higher elevations and their Δ LSTs are often warmer than other pixels with similar elevations in WFR while AWFPs correspond to higher elevation but lower Δ LSTs in NWFR. The similarities between Figures 4a and 4c and between Figures 4b and 4d indicate that our results from the two different methods are robust.

Zhou et al. (Zhou et al. 2012; Zhou et al. 2013) found that the warming effect over wind farms is the smallest in DJF and the strongest in JJA over WFR. Here we apply the EOF analysis (method I) to DJF and ANN and examine how Δ LST changes with elevation as done in Figure 4. For EOF1 in WFR, there is an increase in Δ LST in DJF with elevation, which differs from JJA, and the LSTs in WFPs are only slightly higher than other pixels with similar elevations (Figure 5a). For EOF1 in NWFR, the DJF Δ LST decreases with elevation and the Δ LSTs differ little between AWFPs and other pixels with similar elevations (Figure 5a). The Δ LST differences between the averages of 2009–11 and those of 2003–05 (Figure 5b) are similar to those in EOF1 (Figure 5a). As expected, the results of ANN show similar features as those in JJA but with a smaller magnitude in terms of Δ LST changes. Again, our two different methods (methods I and II) provide consistent results in both WFR and NWFR.

Results of Figures 4 and 5 show that the Δ LST means between three subgroups of pixels (WFPs, UWFPs, and AWFP) differ from their surroundings pixels with similar elevations. Given the large variation of sample size among different groups and different elevation bins, it is necessary to test (i) whether the Δ LST means of WFPs differ statistically significantly from those of other pixels with similar

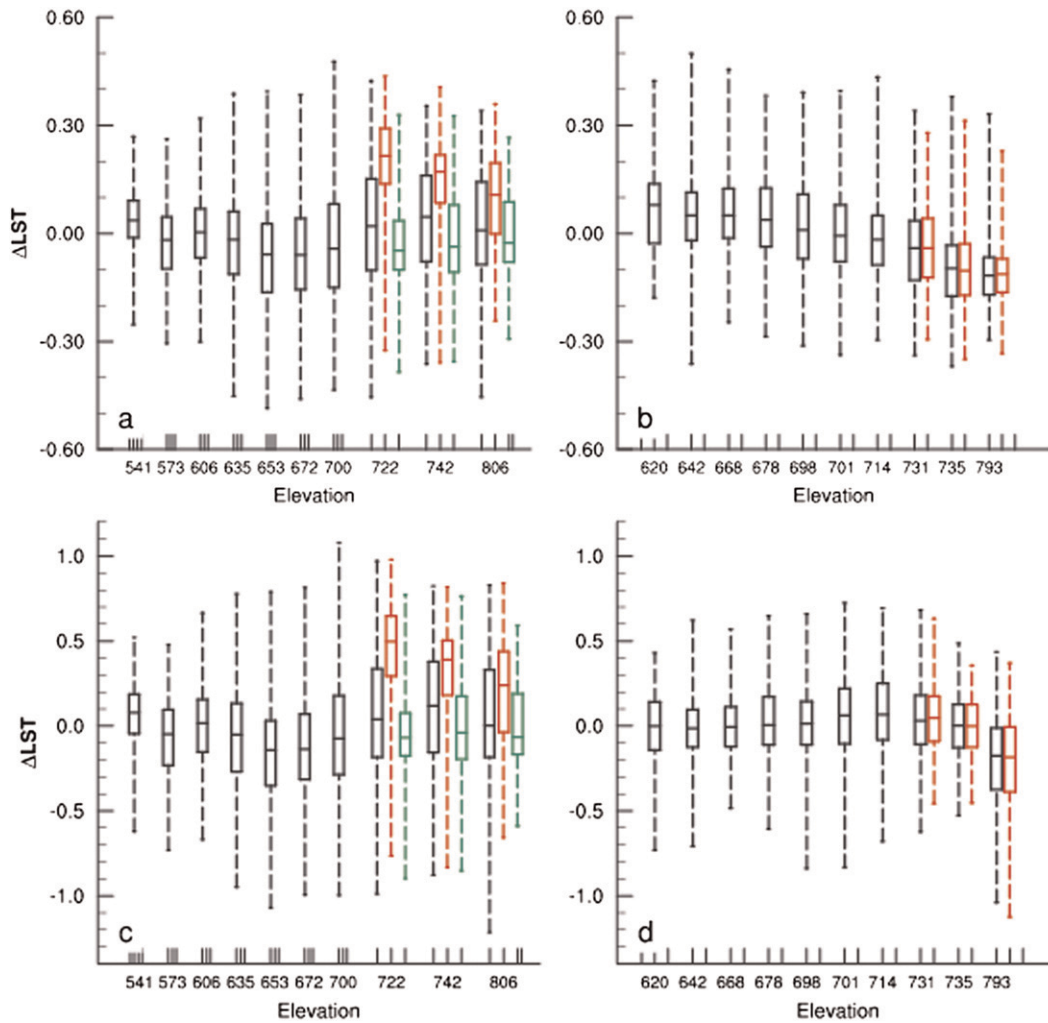


Figure 4. (top) Box-and-whisker chart of EOF1 of MODIS JJA nighttime ΔLST (°C) in (a) WFR and (b) NWFR as a function of elevation (m) at pixel level. All the pixels are divided evenly into 10 elevation bins. WFPs in WFR and AWFPs in NWFR are in red and UWFPs are in green. For each elevation bin, if WFPs and UWFPs are present, the chart in black represents all of the pixels for each bin excluding WFPs in WFR. Similarly, if AWFPs are present, the chart in black represents all of the pixels for each bin excluding AWFPs in NWFR. (bottom) As in (top), but for the MODIS JJA nighttime ΔLST differences (°C) (2009–11 minus 2003–05 averages).

elevations or from UWFPs in WFR and (ii) whether the ΔLST means of AWFPs differ statistically significantly from those of other pixels with similar elevations in NWFR. Table 1 lists the mean, standard deviation (STD), and pixel numbers of each group of pixels for three elevation bins: 722, 742, and 806 in WFR and 731, 735, and 793 in NWFR. Evidently, WFPs differ statistically significantly at the 1% level in their ΔLST means from their surrounding pixels with similar elevations

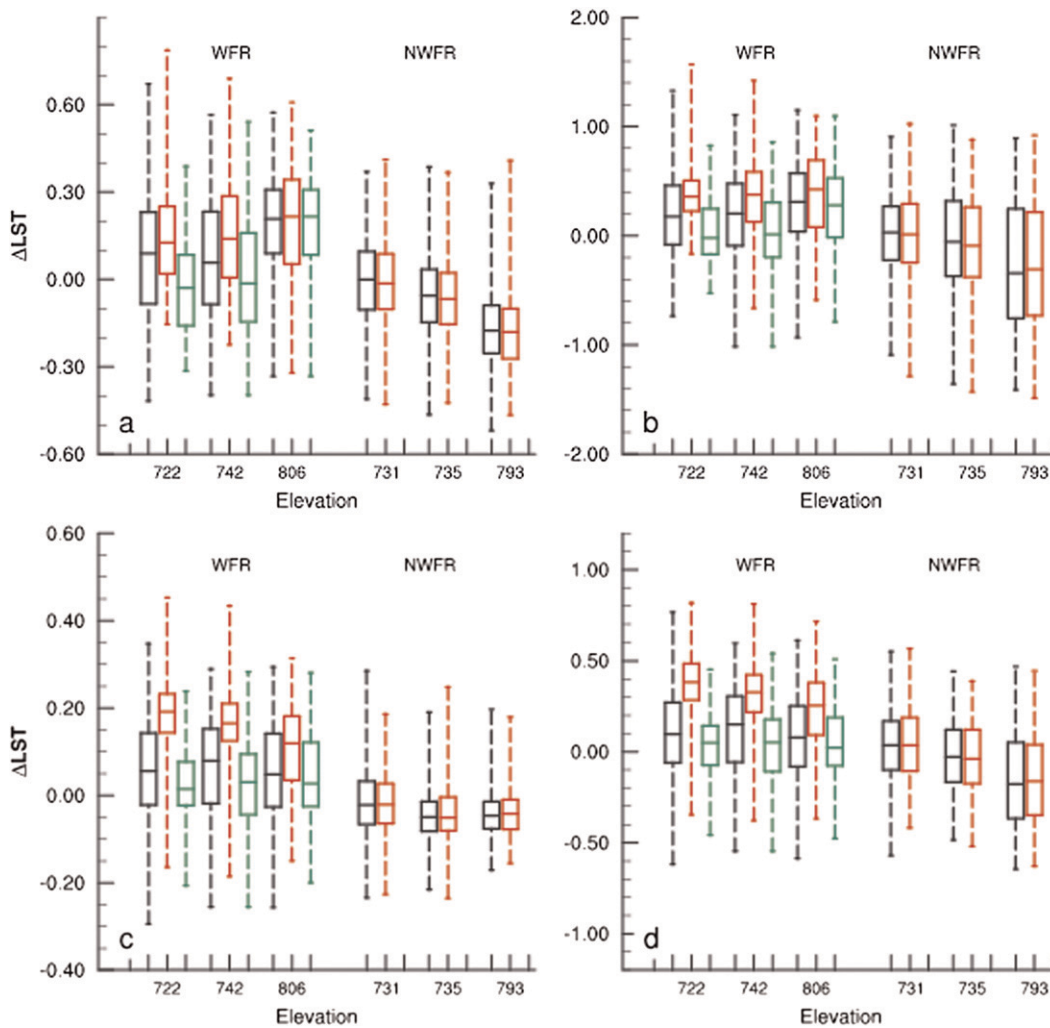


Figure 5. (top) Box-and-whisker chart of MODIS DJF nighttime ΔLST (°C) in WFR and NWFR from (a) EOF1 and (b) the differences (2009–11 minus 2003–05 averages) using method II as a function of elevation (m) at pixel level. The elevation bins and colors are defined as in Figure 4. (bottom) As in (top), but for MODIS ANN nighttime ΔLST .

and from UWFPs for almost all of the 18 cases (3 elevation bins \times 3 seasons \times 2 methods). The only exception is the case for the highest-elevation bin (806 m) in DJF, which is expected as the wind farm impact is the weakest in DJF (Zhou et al. 2012). It is interesting to note that the ΔLST differences between WFPs and their surrounding pixels with similar elevations or between WFPs and UWFPs become smaller with the increase of elevation, which is also seen in Figures 4 and 5, suggesting that the impact of wind farms decreases with elevation. In NWFR, the ΔLST means of AWFPs are not different statistically from those of their surrounding pixels with similar elevations for all of the 18 cases, even at the 10% significance level.

Table 1. Statistical significance of LST differences between the means of different groups of pixels in WFR and NWFR.

WFR										
Elevation bins										
Pixel groups*	722			742			806			
	Mean**	STD	Pixels	Mean**	STD	Pixels	Mean**	STD	Pixels	
NWFPs	0.02	0.16	741	0.04	0.16	659	0.01	0.16	594	Figure 4a
WFPs	0.21	0.11	199	0.14	0.12	294	0.10	0.13	343	
UWFPs	<i>-0.03</i>	0.11	151	<i>-0.02</i>	0.13	388	0.00	0.12	359	
NWFPs	0.05	0.36	741	0.10	0.36	659	0.02	0.39	594	Figure 4c
WFPs	0.46	0.25	199	0.32	0.29	294	0.20	0.31	343	
UWFPs	<i>-0.05</i>	0.25	151	<i>-0.03</i>	0.29	388	0.00	0.25	359	
NWFPs	0.08	0.22	741	0.07	0.20	659	0.18	0.17	594	Figure 5a
WFPs	0.16	0.18	199	0.15	0.19	294	0.19	0.20	343	
UWFPs	<i>-0.02</i>	0.17	151	0.01	0.20	388	0.18	0.18	359	
NWFPs	0.20	0.37	741	0.18	0.37	659	0.29	0.37	594	Figure 5b
WFPs	0.41	0.30	199	0.38	0.35	294	0.39	0.39	343	
UWFPs	0.05	0.30	151	0.06	0.37	388	0.24	0.36	359	
NWFPs	0.05	0.12	741	0.06	0.11	659	0.05	0.12	594	Figure 5c
WFPs	0.19	0.07	199	0.16	0.09	294	0.11	0.10	343	
UWFPs	0.03	0.08	151	0.03	0.10	388	0.05	0.10	359	
NWFPs	0.10	0.23	741	0.12	0.24	659	0.07	0.24	594	Figure 5d
WFPs	0.38	0.16	199	0.31	0.18	294	0.24	0.20	343	
UWFPs	0.04	0.16	151	0.04	0.21	388	0.05	0.19	359	
NWFR										
Elevation bins										
Pixel groups*	731			735			793			
	Mean**	STD	pixels	Mean**	STD	pixels	Mean**	STD	pixels	
NAWFPs	-0.04	0.12	670	-0.09	0.11	666	-0.11	0.09	654	Figure 4b
AWFPs	-0.04	0.11	290	-0.09	0.12	296	-0.11	0.09	304	
NAWFPs	0.03	0.21	670	0.00	0.18	666	-0.21	0.29	654	Figure 4d
AWFPs	0.04	0.21	290	-0.01	0.18	296	-0.20	0.28	304	
NAWFPs	-0.01	0.15	670	-0.05	0.14	666	-0.17	0.14	654	Figure 5a
AWFPs	-0.02	0.15	290	-0.06	0.14	296	-0.17	0.14	304	
NAWFPs	0.03	0.34	670	-0.05	0.47	666	-0.28	0.58	654	Figure 5b
AWFPs	0.02	0.38	290	-0.06	0.44	296	-0.27	0.57	304	
NAWFPs	-0.02	0.07	670	-0.05	0.06	666	-0.04	0.05	654	Figure 5c
AWFPs	-0.02	0.07	290	-0.04	0.07	296	-0.04	0.06	304	
NAWFPs	0.03	0.19	670	-0.02	0.19	666	-0.15	0.25	654	Figure 5d
AWFPs	0.03	0.20	290	-0.03	0.19	296	-0.16	0.25	304	

* NWFPs refer to all of the pixels for each bin that are not WFPs in WFR, and NAWFPs refer to all of the pixels for each bin that are not AWFPs in NWFR; WFPs, UWFPs, and AWFPs are defined in the main text.

** The LST differences between NWFPs and WFPs in bold or between UWFPs and WFPs in italic bold are statistically significant at the 1% level. None of the LST differences between NAWFP and AWFPs is statistically significant even at the 10% level. A two-tailed Student's *t* test was used to test whether the LST mean differs significantly.

Next we quantify the impacts of wind farms on ΔLST by estimating the total trend (method III) for the areal mean ΔLST differences $\overline{\Delta LST}$ between WFPs (AWFPs) and their nearby nonwind farm pixels for WFR (NWFR) as done in Zhou et al. (Zhou et al. 2012). Note that $\overline{\Delta LST}$ contains the ΔLST change due to the differences in not

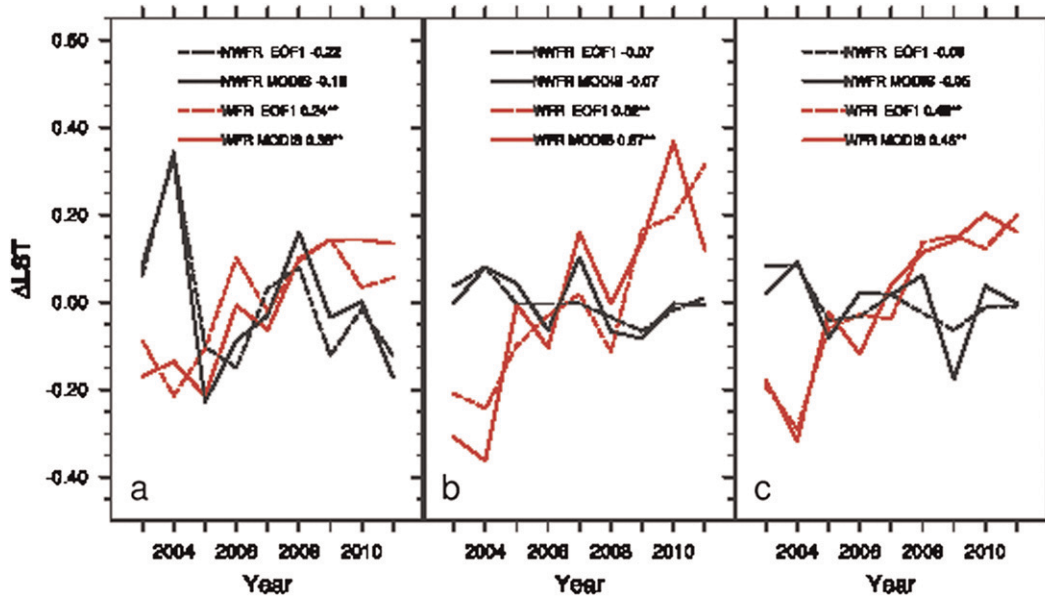


Figure 6. Time series of $\overline{\Delta LST}$ (i.e., areal mean MODIS nighttime ΔLST difference) ($^{\circ}\text{C}$) between WFPs (AWFPs) and their nearby nonwind farm pixels in WFR (NWFR) in (a) DJF, (b) JJA, and (c) ANN for the period of 2003–11. Here, the MODIS plots refer to the $\overline{\Delta LST}$ difference estimated using MODIS ΔLST s and the EOF1 plots refer to the same $\overline{\Delta LST}$ difference but using the reconstructed EOF1 time series only. Total trends ($^{\circ}\text{C}$ per 8 yr) are listed in the figure legends and those with two asterisks (one asterisk) are statistically significant at the 1% (5%) level. WFPs, AWFPs, and total trend are defined in the main text.

only elevation but also land surface properties between WFPs/AWFPs and their nearby nonwind farm pixels. However, method III examines how $\overline{\Delta LST}$ changes temporally with the development of wind farms while the land surface properties do not change much with time (Zhou et al. 2012). In addition, its p values can tell whether the trends are statistically significant from zero. In general, there is a warming effect in WFPs relative to their nearby nonwind farm pixels and this effect increases with time over WFR, while NWFR shows much smaller $\overline{\Delta LST}$ between AWFPs and their nearby nonwind farm pixels (Figure 6). DJF shows the smallest signal of wind farm impacts compared to JJA and ANN, which is consistent with Zhou et al. (Zhou et al. 2012; Zhou et al. 2013). The MODIS ΔLST show a total warming trend of 0.38°C in DJF, 0.57°C in JJA, and 0.46°C in ANN for the 8-yr interval of the study period 2003–11. The reconstructed values using EOF1 and its time series shows a total warming trend of 0.24°C in DJF, 0.52°C in JJA, and 0.45°C in ANN. Although there are only 9 years of data, the total trends are all statistically significant at the 1% level. In contrast, the total trends for NWFR are small except DJF, but none are statistically significant even at the 10% level.

The nighttime EOF1 mode of warmer ΔLST s resembles the geographic patterns of wind turbines that are located at higher-elevation ridges in WFR while the

warmer Δ LSTs are observed over lower-elevation plains and valleys in NWFR. This contrast indicates a possible link between the warming effect over WFPs and the development of wind farms. The gradual strengthening of the spatial coupling of EOF1 mode with wind turbines in WFR is expected, as wind turbines were constructed in stages, with more wind turbines built and likely operating with time from 2003 to 2011. This spatial coupling does not imply causation. However, Zhou et al. (Zhou et al. 2012; Zhou et al. 2013) have examined possible contributors to the LST changes and found that the diurnal and seasonal variations in wind speed and the changes in near-surface ABL conditions due to wind farm operations are likely the primary causes.

4. Conclusions

This paper applies the empirical orthogonal function (EOF) analysis to decompose satellite-derived nighttime land surface temperature (LST) for the period of 2003–11 into spatial patterns of different scales and thus to identify whether (i) there is a pattern of LST change associated with the development of wind farms and (ii) the warming effect over wind farms reported previously is an artifact of varied surface topography. The spatial pattern and time series analysis approaches of Zhou et al. (Zhou et al. 2012; Zhou et al. 2013) are also used to supplement and compare with the EOF results. Two equal-sized regions with similar topography in west-central Texas are chosen to represent a wind farm region (WFR) and a nonwind farm region (NWFR).

Our results indicate that the nighttime warming effect seen in the first mode (EOF1) in WFR very likely represents the wind farm impacts as its spatial pattern couples very well with the geographic distribution of wind turbines, which are generally built on high-elevation ridges. The time series associated with the EOF1 mode in WFR also shows a persistent upward trend over wind farms from 2003 to 2011, corresponding to the increase of operating wind turbines with time. Also, the wind farm pixels show distinctly warmer LST changes from their upwind high-elevation pixels and their downwind nonwind farm pixels at similar elevations. It is interesting to note that the warming effect of wind farms decreases with elevation. In contrast, NWFR shows a decrease in LST with elevation, indicating that the presence of wind farms in WFR has changed the LST–elevation relationship shown in NWFR. The elevation impacts on MODIS LST, if any, are much smaller and statistically insignificant than the strong and persistent signal of wind farm impacts. While the MODIS data may be too short to draw any definite conclusions, these results are consistent with those in Zhou et al. (Zhou et al. 2012; Zhou et al. 2013) and provide further observational evidence of the impacts of wind farms on LST. They also indicate that EOF analysis helps to decompose the MODIS LSTs into different spatial patterns and thus can be used to detect and quantify the impacts of wind farms at local scales.

Acknowledgments. We are grateful to two anonymous reviewers for their constructive comments, which have helped to substantially improve the paper. This study was supported by the startup funds provided by University at Albany, State University of New York and by National Science Foundation (NSF AGS-1247137). H. Chen was supported by the National Basic Research Program of China (Grant 2011CB952000). Y. Dai was supported

by the National Natural Science Foundation of China under Grant 40875062 and the 111 Project of Ministry of Education and State Administration for Foreign Experts Affairs of China.

References

- AWEA, 2012: The AWEA U.S. wind industry annual market report year ending 2011. American Wind Energy Association Rep., 94 pp.
- Baidya Roy, S., and J. J. Traiteur, 2010: Impacts of wind farms on surface air temperatures. *Proc. Natl. Acad. Sci. USA*, **107**, 17 899–17 904.
- Bjornsson, H., and S. A. Venegas, 1997: A manual for EOF and SVD analyses of climatic data. McGill University CCGCR Rep. 97-1, 54 pp. [Available online at <http://www.geog.mcgill.ca/gec3/wp-content/uploads/2009/03/Report-no.-1997-1.pdf>.]
- Fiedler, B. H., and M. S. Bukovsky, 2011: The effect of a giant wind farm on precipitation in a regional climate model. *Environ. Res. Lett.*, **6**, 045101, doi:10.1088/1748-9326/6/4/045101.
- Fitch, A. C., J. K. Lundquist, and J. B. Olson, 2013: Mesoscale influences of wind farms throughout a diurnal cycle. *Mon. Wea. Rev.*, **141**, 2173–2198.
- Imhoff, M. L., P. Zhang, R. E. Wolfe, and L. Bounoua, 2010: Remote sensing of the urban heat island effect across biomes in the continental USA. *Remote Sens. Environ.*, **114**, 504–513.
- Jin, M., and R. E. Dickinson, 2002: New observational evidence for global warming from satellite. *Geophys. Res. Lett.*, **29**, doi:10.1029/2001GL013833.
- Karl, T. R., and Coauthors, 2012: U.S. temperature and drought: Recent anomalies and trends. *Eos, Trans. Amer. Geophys. Union*, **93**, 473, doi:10.1029/2012EO470001.
- Keith, D. W., J. F. DeCarolis, D. C. Denkenberger, D. H. Lenschow, S. L. Malyshev, S. Pacala, and P. J. Rasch, 2004: The influence of large-scale wind power on global climate. *Proc. Natl. Acad. Sci. USA*, **101**, 16 115–16 120.
- Kirk-Davidoff, D. B., and D. W. Keith, 2008: On the climate impact of surface roughness anomalies. *J. Atmos. Sci.*, **65**, 2215–2234.
- Lipton, A. E., and J. M. Ward, 1997: Satellite-view biases in retrieved surface temperatures in mountain areas. *Remote Sens. Environ.*, **60**, 92–100.
- Liu, Y., Y. Noumi, and Y. Yamaguchi, 2009: Discrepancy between ASTER- and MODIS-derived land surface temperatures: Terrain effects. *Sensors*, **9**, 1054–1066, doi:10.3390/s90201054.
- Minder, J. R., P. W. Mote, and J. D. Lundquist, 2010: Surface temperature lapse rates over complex terrain: Lessons from the Cascade Mountains. *J. Geophys. Res.*, **115**, D14122, doi:10.1029/2009JD013493.
- NRC, 2007: *Environmental Impacts of Wind-Energy Projects*. National Academies Press, 377 pp.
- Pacala, S., and R. Socolow, 2004: Stabilization wedges: Solving the climate problem for the next 50 years with current technologies. *Science*, **305**, 968–972, doi:10.1126/science.1100103.
- Pryor, S. C., and R. J. Barthelmie, 2011: Assessing climate change impacts on the near-term stability of the wind energy resource over the United States. *Proc. Natl. Acad. Sci. USA*, **108**, 8167–8171.
- Rajewski, D. A., and Coauthors, 2013 Crop Wind Energy Experiment (CWEX): Observations of surface-layer, boundary layer, and mesoscale interactions with a wind farm. *Bull. Amer. Meteor. Soc.*, **94**, 655–672.
- U.S. DOE, 2008: 20% wind by 2030: Increasing wind energy's contribution to U.S. electricity supply. U.S. Department of Energy Rep., 27 pp. [Available online at <http://www1.eere.energy.gov/wind/pdfs/42864.pdf>.]
- , 2012: Electric power monthly May 2012: With data for March 2012. U.S. Department of Energy Energy Information Administration Rep. DOE/EIA-0226 (2012/03), 180 pp. [Available online at http://www.eia.gov/electricity/monthly/current_year/may2012.pdf.]
- Wan, Z., 2006: New refinements and validation of the MODIS land surface temperature/emissivity products. *Remote Sens. Environ.*, **112**, 59–74.

- , and Z.-L. Li, 1997: A physics-based algorithm for retrieving land-surface emissivity and temperature from EOS/MODIS data. *IEEE Trans. Geosci. Remote Sens.*, **35**, 980–996.
- Wang, C., and R. G. Prinn, 2010: Potential climatic impacts and reliability of very large-scale wind farms. *Atmos. Chem. Phys.*, **10**, 2053–2061.
- Zhang, P., M. L. Imhoff, R. E. Wolfe, and L. Bounoua, 2010: Urban heat island effect across biomes in the continental USA. *Proc. Int. Geoscience and Remote Sensing Symp.*, Honolulu, HI, IEEE, 1920–1923, doi:10.1109/IGARSS.2010.5653907.
- Zhou, L., C. J. Tucker, R. K. Kaufmann, D. Slayback, N. V. Shabanov, and R. B. Myneni, 2001: Variations in northern vegetation activity inferred from satellite data of vegetation index during 1981 to 1999. *J. Geophys. Res.*, **106** (D17), 20 069–20 083.
- , Y. Tian, S. Baidya Roy, C. Thorncroft, L. F. Bosart, and Y. Hu, 2012: Impacts of wind farms on land surface temperature. *Nat. Climate Change*, **2**, 539–543.
- , ——, ——, Y. Dai, and H. Chen, 2013: Diurnal and seasonal variations of wind farm impacts on land surface temperature over western Texas. *Climate Dyn.*, **41**, 307–326, doi:10.1007/s00382-012-1485-y.

Earth Interactions is published jointly by the American Meteorological Society, the American Geophysical Union, and the Association of American Geographers. Permission to use figures, tables, and *brief* excerpts from this journal in scientific and educational works is hereby granted provided that the source is acknowledged. Any use of material in this journal that is determined to be “fair use” under Section 107 or that satisfies the conditions specified in Section 108 of the U.S. Copyright Law (17 USC, as revised by P.L. 94-553) does not require the publishers’ permission. For permission for any other form of copying, contact one of the copublishing societies.
